Published in final edited form as:
Magn Reson Med. 2009 April ; 61(4): 842–850. doi:10.1002/mrm.21896.

Magnetic Resonance Diffusion Characteristics of Histologically Defined Prostate Cancer in Humans

Junqian Xu[1], **Peter A. Humphrey**[2], **Adam S. Kibel**[3,4,5], **Abraham Z. Snyder**[6,7], **Vamsidhar R. Narra**[6], **Joseph J.H. Ackerman**[1,5,6,8], and **Sheng-Kwei Song**[6,*]

[1]Department of Chemistry, Washington University, St. Louis, Missouri.

[2]Department of Pathology and Immunology, Washington University, St. Louis, Missouri.

[3]Department of Surgery, Washington University, St. Louis, Missouri.

[4]Department of Genetics, Washington University, St. Louis, Missouri.

[5]Siteman Cancer Center, Washington University, St. Louis, Missouri.

[6]Department of Radiology, Washington University, St. Louis, Missouri.

[7]Department of Neurology, Washington University, St. Louis, Missouri.

[8]Department of Internal Medicine, Washington University, St. Louis, Missouri.

Abstract

The contrast provided by diffusion-sensitive magnetic resonance offers the promise of improved tumor localization in organ-confined human prostate cancer (PCa). Diffusion tensor imaging (DTI) measurements of PCa were performed in vivo, in patients undergoing radical prostatectomy, and later, ex vivo, in the same patients' prostatectomy specimens. The imaging data were coregistered to histological sections of the prostatectomy specimens, thereby enabling unambiguous characterization of diffusion parameters in cancerous and benign tissues. Increased cellularity, and hence decreased luminal spaces, in peripheral zone PCa led to approximately 40% and 50% apparent diffusion policy (ADC) decrease compared with benign peripheral zone tissues in vivo and ex vivo, respectively. In contrast, no significant diffusion anisotropy differences were observed between the cancerous and noncancerous peripheral zone tissues. However, the dense fibromuscular tissues in prostate, such as stromal tissues in benign prostatic hyperplasia in central gland, exhibited high diffusion anisotropy. A tissue classification method is proposed to combine DTI and T2-weighted image contrasts that may provide improved specificity of PCa detection over T2-weighted imaging alone. PCa identified in volume rendered MR images qualitatively correlates well with histologically determined PCa foci.

Keywords

prostate carcinoma (PCa); diffusion tensor imaging (DTI); apparent diffusion coefficient (ADC); fractional anisotropy (FA)

Prostate cancer (PCa) is the leading malignancy and the second most common cause of cancer death in American men (1). Current curative strategies focus on the detection and

*Correspondence to: Sheng-Kwei Song, Biomedical MR Laboratory, Department of Radiology, Campus Box 8227, Washington University School of Medicine, 4525 Scott Avenue, St. Louis, MO 63110. ssong@wustl.edu.

treatment of early-stage tumors (2). The standard method of diagnosis, transrectal ultrasound guided needle biopsy, misses 20–30% of clinically significant tumors (3). A noninvasive imaging method to accurately localize PCa could guide targeted biopsy and theoretically decrease the false-negative rate of needle biopsy. In addition, accurate tumor localization within the prostate would enable focal therapies using cryosurgery (4), intensity modulated radiation therapy (IMRT) (5), brachytherapy (6), or high intensity focused ultrasound (HIFU) (7) to effect a "partial prostatectomy" (to ablate just the tumor).

Current MRI evaluation of PCa primarily relies on multi-planar T2-weighted (T2w) contrast, which is not sensitive or specific enough for accurate PCa localization (2,8). Other promising MR methods are being pursued. For example, the ^{1}H MR spectroscopy (MRS) determined choline + creatine to citrate resonance intensity ratio has been shown to be a predictive molecular signature of PCa (9). Dynamic contrast enhanced (DCE) MRI has also been explored to evaluate the microvasculature characteristics of PCa, including vascular volume and permeability (10,11). Both MRS and DCE MRI have been used to complement T2w imaging. However, neither method currently provides image resolution sufficient for practical tumor localization.

Diffusion-sensitive MR imaging, with higher resolution than the MRS and DCE MRI, also holds promise for improved PCa localization. The apparent diffusion coefficient (ADC) and diffusion anisotropy of water, parameters derived from diffusion tensor imaging (DTI), reflect tissue microstructure at the micron scale and hence are sensitive to pathologic changes (12). In an earlier study from this laboratory, the markedly lower ADC of PCa compared with normal prostate provided greatly improved contrast of PCa versus noncancerous prostate tissue in a transgenic mouse model in vivo (13). The approximately 70% ADC decrease in PCa compared with noncancerous prostate in the mouse has its origins in the distinct microarchitectural features of these tissues. While there are significant differences between the structure of mouse and human prostate, the characteristic ductal branching morphology of normal prostate tissue and the increased cellularity in PCa are the same. Hence, the distinct microarchitectural features leading to decreased ADC in PCa relative to noncancerous prostate should also be present in humans.

Indeed, in vivo diffusion measurements of human prostate have reported a decreased ADC value in suspected cancerous tissues identified by either T2w images or biopsy results (14–21). While such findings are encouraging, wide intersubject and inter-laboratory variability in the reported diffusion indices emphasize the circumstantial (inferential) nature of such observations. Remarkably, the expectation of significantly decreased ADC in human PCa in vivo has yet to be directly confirmed or quantified by means of "gold standard" PCa identification of the suspected lesions through step-section histology and coregistration. Here, for the first time, the MR diffusion characteristics of histologically defined PCa were directly determined and quantified both in vivo, in radical prostatectomy patients before surgery, and, later, ex vivo, in the same patients' prostatectomy specimens post resection. Quantitatively translating earlier findings in a mouse model (13), this work supports the promise of diffusion-sensitive MR for the noninvasive identification and localization of PCa in man.

MATERIALS AND METHODS

Patients

Twenty-four prostate cancer patients scheduled to undergo radical prostatectomy (mean age, 62 years; range, 46–76 years) were recruited for this study. Patients receiving any preoperative treatment, such as androgen ablation or radiation therapy, were excluded. This study was approved by the local Institutional Review Board. Informed consent was obtained

from each patient before the study. The prostates from 14 patients, of which 12 had tumor size greater than 0.1 cc, were examined both in vivo (before surgery) and ex vivo (after resection). The prostates of the other 10 patients, of which 4 had tumor size greater than 0.1 cc, were examined only ex vivo, after resection.

In Vivo MRI

In vivo imaging was performed on a 1.5 Tesla (T) MR scanner (Sonata, Siemens AG, Erlangen, Germany) using a four-channel body phased-array surface coil for signal reception. The whole prostate gland was examined, using both diffusion weighted (DW) and T2w multislice (2.5-mm-thick transverse slices) imaging. DWI was performed using a single shot spin-echo echo planar imaging (SE-EPI) sequence with field of view (FOV) 256 × 256 mm^2, data matrix 128 × 128, partial *k*-space 6/8, TR/TE 4000/76 ms, and diffusion time 30 ms. An acceleration factor of two was used to shorten the EPI echo train length, and hence reduce off-resonance distortions, in the phase encoding direction by means of the generalized autocalibrating partially parallel acquisition (GRAPPA) technique (22). Neither cardiac/peripheral pulse nor respiratory triggering was used. Four image data sets, each consisting of one image with *b* value of 0 s/mm^2 and six diffusion sensitized images on six noncollinear (oblique dual gradient or ODG) diffusion encoding directions with *b* values of 500 s/mm^2, were acquired and the magnitude images averaged (23). Sixteen of these averaged full DWI data sets, each postprocessed to correct for artifacts resulting from eddy currents and motion, were collected and averaged to further improve the signal-to-noise ratio (SNR) (24). Voxel-based ADC and fractional anisotropy (FA) maps were calculated after two-point (i.e., two *b* values) logarithmic fit of the image intensity and diffusion tensor matrix diagonalization (12). The total acquisition time for in vivo DTI was approximately 30 min. T2w images were acquired with a turbo spin echo (TSE) sequence with FOV 256 × 256 mm^2, matrix 256 × 256, echo train length (ETL) 13, and TR/TE 2800/120 ms.

Ex Vivo MRI

After surgery, each prostate specimen was fixed with 10% formalin in phosphate buffered saline (PBS, pH = 7.4) for at least 48 h. The specimen was step-sectioned at 4-mm intervals from base to apex using a laboratory designed and constructed prostate slicer. The step-sectioned slices were re-grouped into a whole prostate with thin plastic spacers placed between each 4-mm slice. The regrouped prostate specimens then were wrapped in a lint-free tissue (Kimwipes, Kimberly-Clark, GA) and placed in a formalin filled plastic bag to hold the slices in place and to prevent tissue dehydration. Ex vivo specimens were imaged on a 4.7-tesla MR scanner (console by Varian NMR Systems, Palo Alto, CA; magnet by Oxford Instruments, Oxford, UK; gradients by Magnex Scientific, Oxford, UK) using a 7-cm-diameter quadrature “Litzcage” radio frequency coil (Doty Scientific, Columbia, SC). A multislice spin echo imaging sequence with a pair of diffusion sensitizing pulsed gradients was used to acquire DW images (25). High resolution (500 × 500 × 500 μm^3) images were collected with diffusion time 12 ms, diffusion gradient duration (δ) 4 ms, slice thickness 0.5 mm, FOV 6.5 cm × 6.5 cm, data matrix 128 × 128, TR/TE 6000/35 ms. The number of obtained slices was sufficient to cover each specimen completely. Eight DW image data sets, each consisting of 12 images with two *b* values of 45 and 1130 s/mm^2 on six noncollinear (oblique dual gradient or ODG) diffusion encoding directions, were averaged in the complex *k*-space (23). The magnitude images of the averaged data were used to calculate ADC and FA maps by standard procedures as for the in vivo experiments (12). The total acquisition time for ex vivo DTI was approximately 12 h. T2w images were acquired with a multi-slice SE sequence with FOV 6.5 × 6.5 mm^2, data matrix 128 × 128, and TR/TE 5000/60 ms.

Histology

After ex vivo MRI data was acquired, each 4-mm slice from the resected specimen was cut into halves or into quarters depending on the size of each slice and embedded in paraffin. A 4-μm slice was obtained parallel to the MR imaging plane for hematoxylin and eosin (H&E) staining. Regions of PCa and benign prostatic hyperplasia (BPH) were delineated in blue/black and red, respectively, on all H&E-stained slides by an experienced urologic pathologist (P.A.H.) blinded to the MR imaging results. The intraglandular tumor extent, reported as volume percentage of the gland containing carcinoma, was determined by grid morphometry (26). Histology slides from half-cut or quarter-cut specimens were later digitized and reassembled together into whole cross-sectional slices. The tumor sizes were then determined by counting the pixels in each identified PCa foci. Regions of BPH (of size larger than 0.1 cc) containing predominantly fibromuscular or epithelial cells were identified as stromal or epithelial BPH, respectively, on the digitized slides.

MR/Histology Image Coregistration

The plane of histology section of the specifically sliced prostatectomy specimens was closely matched to the slice plane of the ex vivo MR images. To account for histological slicing and mounting distortions, a two-dimensional (2D) thin plate spline (TPS) warping was performed using 20–30 control points to correct the histology image coordinates to the coordinates of ex vivo MR images using ImageJ (NIH, Bethesda, MD) software (27,28). Using a rigid body three-dimensional (3D) affine transformation with 9 degrees of freedom (DOF), each ex vivo ADC and FA map was further transformed into the coordinate of the corresponding in vivo T2w image based on the manual alignment of intragladular structures using the ITK registration module in Analyze (Mayo Clinic, Rochester, MN) software. The final step coregistering the in vivo ADC and FA maps to the in vivo T2w images was accomplished by using an unsupervised 3D affine transformation with 12 DOF and laboratory developed software (24). As summarized in Figure 1, a match of alignment (orientation and position) between histology slides and in vivo ADC and FA slices in the standard in vivo T2w image space was achieved. The histologically identified tissue types were thus mapped onto the in vivo MR images. A tumor size threshold of 0.1 cc was empirically determined as the minimum size to reliably map cancerous tissue regions from histology to MR images. Hence, tumor foci smaller than 0.1 cc were not mapped. This threshold excluded 37 tumor foci from a total of 67 tumor foci. Consequently, eight patients with tumor burden < 5% were excluded from further analysis, which resulted in 16 ex vivo and 12 in vivo cases to define histology-DTI PCa correspondence. After MR and histology image coregistration for each slice, regions of PCa, benign peripheral zone (PZ) tissue, stromal and epithelial BPH were mapped from the histology slide to both the ex vivo and in vivo diffusion images.

Statistical Analysis

Results are presented as mean ± standard deviation (SD). Statistical significance was defined as $P < 0.01$ by the Wilcoxon signed rank tests.

Volume Rendering

Representative ex vivo and in vivo DT images were volume rendered using Amira (Mercury Computer Systems, Richmond, TX) software. The whole prostate gland was segmented from ex vivo or in vivo T2w images. The ADC and FA values were imported into yellow–orange and green–blue channels, respectively. The scales for ADC were inverted for visualization with bright yellow–orange regions in the MR images as carcinoma determined by an upper ADC threshold (mean tumor ADC + SD). The scales for FA were chosen for optimal visualization of fibromuscular tissues. For ex vivo cases, 2D projection images were

taken and ejaculatory ducts were segmented from ADC map separately due to the very high ADC value of the structure (color scale reversed comparing with the prostate tissues). For in vivo cases, the volume rendered images were projected onto representative T2w images.

RESULTS

The 16 patients with tumor size greater than 0.1 cc had postsurgery histology-determined mean tumor burden of 20% (range, 5% to 46%) and a median postresection Gleason score of 3 + 4 = 7 (range, 3 + 3 = 6 to 4 + 5 = 9). There were a total of 67 tumor foci (median size, 1.31 cc; range, 0.51–5.05 cc) identified in histological samples from these 16 patients' prostate specimens. Among all tumor foci, three groups were identified according to size: less than 0.1 cc (n = 37), between 0.1 cc and 0.5 cc (n = 13), and greater than 0.5 cc (n = 17). Nine of the 16 patients had peripheral zone PCa invading the central gland (CG) or PCa originating from the transitional zone (TZ). BPH was present in all but three patients.

For both in vivo and ex vivo measurements, ADC distinguishes PCa from noncancerous PZ tissues (Fig. 2a,c), while FA differentiates stromal from epithelial BPH (Fig. 2b,d).

The ADC value of PCa tissue (0.43 ± 0.06 μm^2/ms ex vivo, Figure 3d yellow arrow, and 0.94 ± 0.14 μm^2/ms in vivo, Fig. 3a yellow arrow) was significantly lower ($P = 0.0005$ ex vivo n = 16, and $P = 0.003$ in vivo n = 12) than that of noncancerous PZ tissues (0.84 ± 0.13 μm^2/ms ex vivo, and 1.66 ± 0.21 μm^2/ms in vivo). The difference between the ADC value of stromal BPH (0.65 ± 0.08 μm^2/ms ex vivo, and 1.28 ± 0.20 μm^2/ms in vivo) was not significant ($P = 0.13$ ex vivo n = 16, and $P = 0.098$ in vivo n = 12) from that of epithelial BPH (0.85 ± 0.44 μm^2/ms ex vivo, and 1.42 ± 0.19 μm^2/ms in vivo). The ADC of BPH (stromal or epithelial) overlaps with that of both PCa and benign PZ tissue.

Nonfibromuscular tissues (PCa, normal prostate, and epithelial BPH) show no significant FA. In addition, no significant diffusion anisotropy differential was observed (peripheral zone, Figs. 3c,f, 4a,c) between the cancerous and noncancerous PZ tissues (FA = 0.23 ± 0.04 vs 0.21 ± 0.06; $P = 0.40$ for ex vivo n = 16; and FA = 0.14 ± 0.04 vs 0.09 ± 0.03, $P = 0.018$ for in vivo n = 12). However, when the fibromuscular cells are bundled together at a length scale comparable to MRI voxel dimensions (Fig. 3i), significantly higher ($P = 0.0002$ ex vivo n = 13, and $P = 0.004$ in vivo n = 9) diffusion anisotropy in those regions, such as stromal BPH (FA = 0.52 ± 0.08 ex vivo and 0.24 ± 0.06 in vivo) becomes distinctive and distinguishable (red arrows, Figs. 3c,f, 4a,c, 5e) from that in the glandular regions, such as epithelial BPH (FA = 0.18 ± 0.05 ex vivo and 0.08 ± 0.01 in vivo).

Finally, to take advantage of the DTI contrasts quantitatively, six representative cases with different tumor burden are presented for ex vivo (Fig. 6) and in vivo (Fig. 7), respectively. The tumor volume and distribution were highlighted in bright orange in the volume rendered and projected DTI images using ADC threshold (mean tumor ADC + SD) and color coding, which correlate well with the corresponding histologically defined extent and stage of the same tumors.

DISCUSSION

Based on our findings, a prostate tissue classification method that combines both DTI and T2w contrasts is proposed (Table 1). The various tissue types contributing to the classification scheme were verified by histological analysis after coregistration. In general, ADC contrast parallels the T2w contrasts with ADC being more specific than T2w contrast for PZ PCa (Fig. 3a,b white arrows). Diffusion anisotropy provides a unique contrast that differentiates stromal BPH from PCa in the CG, while its utility for PZ PCa is limited.

Microscopically, normal prostate has a branching duct–acinar glandular architecture embedded in a dense fibro-muscular stroma (Fig. 3g). This duct–acinar structure underlies the diffusion MR characteristics of the prostate gland in both human and the previously reported mouse model. In prostate carcinoma, tightly packed tumor cells disrupt the duct–acinar structure leading to the decreased ADC in tumor due to the cellularity induced diffusion restriction (Fig. 3h).

The luminal space in benign human prostate is, on average, hundreds of microns wide. Under conditions typical of diffusion-sensitive MR imaging protocols, as in this study with an in vivo diffusion time of 30 ms, it is estimated that water diffuses over a distance of tens of microns. Thus, water in the normal prostate is relatively unrestricted and the ADC measured in humans is fairly high, typically ~1.7 μm^2/ms. (Note: in vivo ADC of ~0.8 μm^2/ms has been reported in normal human brain gray and white matter.) The high cellularity of most PCa presents hindrances and restrictions to water diffusion over a distribution of length scales covering from the sub-micron to tens of microns range. This is the displacement scale to which the MR diffusion imaging is sensitive. Thus, the majority of PCa was found to have a markedly lower ADC in vivo than noncancerous prostate. It is noteworthy that some intermediate grade (e.g., Gleason grade = 3, score = 6) infiltrative PCa does not affect the prostate cellularity; hence, it is not clear whether change in ADC may be expected. This type of PCa may also be of significant clinical relevance and may require other contrast mechanisms or modality to detect.

The nearly twofold in vivo ADC difference between PCa and benign prostate was preserved in formalin-fixed prostatectomy specimens, in agreement with Williams et al. (29). Although the formalin fixation process reduces the ADC for both PCa and normal prostate tissue, the microstructure is largely preserved as evidenced by the comparable ADC decrease observed for PCa relative to noncancerous prostate tissue both in vivo (~ 40%) and ex vivo (~50%). We speculate that further diffusion-sensitive MR studies of radical prostatectomy specimens may provide a correlation between certain MR diffusion signature and tumor grade, which can be translated to in vivo studies.

The ADC value in the human prostate gland is not homogeneous (Fig. 3d). In normal peripheral zone tissues, ADC maps acquired ex vivo usually display bright spots (high ADC values) scattered throughout a relatively uniform background of somewhat lower ADC. We speculate that these high ADC voxels reflect regions with large diameter glandular spaces. This ADC heterogeneity is lost in vivo due to significant partial volume effect and hence not observed under the coarser in vivo MR image resolution (Fig. 3a).

The ADC distribution is even more heterogeneous in the CG, including the transition zone, spanning the complete spectrum of observable ADC values in the prostate ex vivo (Fig. 5d). The presence of BPH, the variation in stromal and epithelial tissue composition, and the formation of cysts in the CG all contribute to the observed wide distribution of ADC values. The appearance of BPH in ADC map (Fig. 5d) or T2w image (Fig. 5f) is also heterogeneous within subject, reflecting the complicated BPH tissue composition. Regions of BPH composed of compact fibromuscular stroma exhibit low ADC values. In optical density measurements, these stromal BPH appears to be similar in tissue density to the closely packed glands in PCa (30). This is likely the cause of the overlap of ADC values between PCa and BPH. On the other hand, BPH dominated by glandular epithelial cell proliferation exhibits heterogeneous ADC contrast. Regions of sparse epithelial BPH components exhibit relatively high ADC values comparable to benign PZ tissues, while regions of compact epithelial BPH components exhibit considerably low ADC values similar to PCa (Fig. 5d). Therefore, the overall BPH ADC-contrast depends on the ratio of the stromal and epithelial components, as well as the compactness of cell packing. As the composition of BPH and CG

is extremely variable and almost always heterogeneous, ADC contrast in CG will vary significantly between different regions in the same patient's prostate and between patients.

The ADC value of BPH overlaps with that of both PCa and benign PZ tissue (Fig. 2a,c). BPH regions with both ADC and T2w hypointensity could mimic PCa (Fig. 3a,b, red arrow), leading to false-positive PCa identification. In such ambiguous cases, high diffusion anisotropy identifies stromal BPH, thus avoiding its false-positive identification as PCa in the CG (Fig. 3c,f, red arrow), which accounts for approximately 30% of all PCa.

The network of fibromuscular connective tissues in the prostate leads to the observed diffusion anisotropy. Relatively high diffusion anisotropy was commonly observed ex vivo in periurethral muscles, anterior fibromuscular regions, stromal BPH or fibrous tissues surrounding the BPH. Notably, the high diffusion anisotropy appears not only in the stromal components within BPH, but also in the fibrous tissues surrounding the BPH (Fig. 5e), as the expanding BPH nodule pushes and compacts the fibromuscular tissue network around it. This high diffusion anisotropy pattern surrounding the BPH is best visualized in the volume rendered DTI images (Fig. 5b).

Nevertheless, the diffusion anisotropy is not particularly evident in the regions dominated by epithelial cells (PCa, normal PZ, and epithelial BPH) with the scale of the MR imaging resolution used herein (Figs. 3f, 4c, 5e, PZ tissues). The low diffusion anisotropy in these regions likely reflects the random orientation of fibromuscular cells (Fig. 3g,h). The anisotropy in prostate is also subject to partial volume averaging. Hence, much lower diffusion anisotropy is observed in vivo (resolution $2 \times 2 \times 2.5\ mm^3$) comparing to that of ex vivo (resolution $0.5 \times 0.5 \times 0.5\ mm^3$). However, patient motion in vivo as well as the formalin fixation caused tissue changes ex vivo may have also contributed to the observed difference. The diffusion anisotropy measurement, which reports the standard deviation of the principal diffusivities, is also sensitive to measurement noise. More specifically, the measured anisotropy is always biased upward with the increased image noise. As SNR is always a concern for the in vivo diffusion imaging experiment, artifactually high diffusion anisotropy due to noise variation is not uncommon (Fig. 3c yellow arrow). This is especially true in the PCa region where shorter T2 leads to significantly reduced SNR than that in the benign tissue regions (31). Microscopically, there is no histological evidence to support an increased density of fibromuscular tissues in PCa. In addition, the fibromuscular cells in PCa, like those in the benign peripheral zone tissues, do not bundle together or show a coherent orientation (Fig. 3h). Such random microarchitecture is unlikely to result in increased diffusion anisotropy under the present imaging conditions. Thus, we did not observe a significant anisotropy differential between the PCa and non-PCa peripheral zone tissues, neither ex vivo nor in vivo. This latter negative finding is in contrast to the positive results reported by Gibbs et al., and the preliminary findings on pre and post hormone/radiation therapy PCa patients by Vigneron et al. and Chen et al., respectively, where significant anisotropy contrast between these tissues were reported (21,32,33). Sinha and Sinha reported even higher values of anisotropy (mean FA range 0.41–0.50) for both the peripheral zone and central gland tissue in a study of volunteers (34). Although age differences could be a confounding factor, such high diffusion anisotropy is likely due to artifactual noise variation, as reported by Reinsberg et al., who evaluated effects of SNR on diffusion anisotropy in human prostate in vivo (35). The low diffusion anisotropy of PCa and non-PCa peripheral zone tissues reported in the present study are in agreement with the preliminary reports by Reinsberg et al. using an EPI diffusion sequence, Haker et al. and Roebuck et al. using a line-scan diffusion sequence, and Vigneron et al. using a fast spin-echo diffusion sequence (33,35–37). Considering the technical constraints encountered with in vivo body diffusion imaging, accurate diffusion anisotropy measurements in human prostate in vivo remain a challenge.

The precise coregistration using histologically identified PCa used in this study avoids the uncertainty of in vivo T2w image region of interest (ROI) placement and/or the sampling error of needle biopsy. Such methodological differences likely explain the approximately 30% lower in vivo PCa mean ADC value (0.99 μm^2/ms) reported herein compared with that reported for suspected PCa by others (range, 1.27–1.43 μm^2/ms) (19). This may also account for the relatively small variations of ADC values in cancerous tissues between patients in our study and a clear ADC value separation between PCa and benign PZ tissues. The coregistration error is a concern in the current study for the manual registration step used to translate the ex vivo coordinates to the in vivo space. Nevertheless, the patients recruited in this study (mean age 62 years) commonly harbor large amounts of BPH, and cysts. These intraglandular landmarks, easily identified in both in vivo T2w image, and ex vivo ADC or FA map, facilitated the manual coregistration procedure. Such landmarks also help to guide the placement of control points in both histology slides and corresponding ex vivo MR images to achieve an accurate warping of the histology slide into the ex vivo MR coordinate. The latter could be performed more accurately using whole-mount histology slides. Additionally, the entire coregistration procedure could be optimized by using mutual information-based automatic procedures such as that reported by Meyer et al. (38).

A phased-array body receiver coil was used for in vivo MR data acquisition in this study instead of an endorectal receiver coil. The limited signal sensitivity of the phased-array body receiver coil for the prostate gland residing at the center of the abdomen mandated significant signal averaging, thus, a prolonged scan time. The relatively small *b* value (500 s/mm^2) was used in consideration of the relatively insensitive signal reception, low magnetic field strength (1.5T scanner), and the expected relatively high benign prostate tissue ADC. The use of an endorectal receiver coil would yield much higher signal sensitivity for the prostate. Hence, the improved diffusion image quality would yield more reliable DTI measurements in vivo and better tissue classification by the proposed method. In addition, the air-filled balloon housing the endorectal coil would serve to immobilize the prostate, hence reducing motion induced image artifacts and blurring. Both of these features would be particularly useful for in vivo diffusion studies, especially diffusion anisotropy measurements. While these advantages are significant, the increased area of air/tissue interface encountered when using an endorectal coil would likely introduce magnetic susceptibility related image artifacts in EPI-based diffusion sequences. Localized shimming procedures and filling the balloon with susceptibility matching fluid, such as a perfluro-carbon, would serve to alleviate the magnetic field inhomogeneity problem. Diffusion pulse sequences such as line-scan or fast spin-echo (33,35–37), though less SNR efficient than EPI, could also be used to reduce these susceptibility based artifacts.

No triggering was used with the single-shot EPI diffusion sequence in this study, although some studies recommend pulse/cardiac gating (34). The single-shot nature of the acquisition and the motion correction procedures used during postprocessing minimizes the effect of bulk or slow body motion, while fast motion on the order of hundreds of milliseconds was not deemed significant for prostate. Considering the relatively distant location from the heart, the prostate is unlikely susceptible to pulsatile motion. Alternatively, respiratory gating or breath-hold acquisition may be practical for use with endorectal coil acquisition, where the decreased scan efficiency is compensated by the improved SNR.

In summary, we report diffusion properties, ADC and anisotropy, of histologically defined PCa in vivo and ex vivo. The good correlation between histology and volume rendered in vivo and ex vivo diffusion images suggests that the ADC threshold may provide a method for PCa volume estimation and tumor staging in the peripheral zone. Exploiting indices such as ADC and diffusion anisotropy is a valuable complement to the conventional T2w imaging for PCa detection.

Acknowledgments

We thank Mattew Budde for providing us the histology ex vivo MRI co-registration software. The constructive comments from the reviewers are highly appreciated.

Grant sponsor: Washington University Small Animal Imaging Resource - a NCI funded Small Animal Imaging Resource Program facility; Grant number: R24 CA83060; Grant sponsor: Small Animal Imaging Core of the Alvin J. Siteman Cancer Center - a NCI Comprehensive Cancer Center; Grant number: P30 CA91842; Grant sponsor: NINDS center core grant; Grant number: P30 NS048056; Grant sponsor: U.S. Army DOD Prostate Cancer Program Pre-doctoral Fellowship; Grant number: PC050667; Grant sponsor: Midwest Stone Institute.

REFERENCES

1. Jemal A, Siegel R, Ward E, Murray T, Xu J, Smigal C, Thun MJ. Cancer statistics, 2006. CA Cancer J Clin. 2006; 56:106–130. [PubMed: 16514137]
2. Kantoff, PW.; Rarroll, PR.; D'Amico, AV., editors. Prostate cancer: principles & practice. 1st ed.. Philadelphia: Lippincott Williams & Wilkins; 2002. p. 278-280.
3. Keetch DW, Catalona WJ, Smith DS. Serial prostatic biopsies in men with persistently elevated serum prostate specific antigen values. J Urol. 1994; 151:1571–1574. [PubMed: 7514690]
4. Katz AE, Rewcastle JC. The current and potential role of cryoablation as a primary therapy for localized prostate cancer. Curr Oncol Rep. 2003; 5:231–238. [PubMed: 12667421]
5. Guckenberger M, Flentje M. Intensity-modulated radiotherapy (IMRT) of localized prostate cancer: a review and future perspectives. Strahlenther Onkol. 2007; 183:57–62. [PubMed: 17294108]
6. Cesaretti JA, Stone NN, Skouteris VM, Park JL, Stock RG. Brachytherapy for the treatment of prostate cancer. Cancer J. 2007; 13:302–312. [PubMed: 17921729]
7. Rouviere O, Souchon R, Salomir R, Gelet A, Chapelon JY, Lyonnet D. Transrectal high-intensity focused ultrasound ablation of prostate cancer: effective treatment requiring accurate imaging. Eur J Radiol. 2007; 63:317–327. [PubMed: 17689218]
8. Coakley FV, Qayyum A, Kurhanewicz J. Magnetic resonance imaging and spectroscopic imaging of prostate cancer. J Urol. 2003; 170:S69–S75. discussion S75–S66. [PubMed: 14610414]
9. Kurhanewicz J, Swanson MG, Nelson SJ, Vigneron DB. Combined magnetic resonance imaging and spectroscopic imaging approach to molecular imaging of prostate cancer. J Magn Reson Imaging. 2002; 16:451–463. [PubMed: 12353259]
10. Padhani AR, Gapinski CJ, Macvicar DA, Parker GJ, Suckling J, Revell PB, Leach MO, Dearnaley DP, Husband JE. Dynamic contrast enhanced MRI of prostate cancer: correlation with morphology and tumour stage, histological grade and PSA. Clin Radiol. 2000; 55:99–109. [PubMed: 10657154]
11. Engelbrecht MR, Huisman HJ, Laheij RJ, Jager GJ, van Leenders GJ, Hulsbergen-Van De Kaa CA, de la Rosette JJ, Blickman JG, Barentsz JO. Discrimination of prostate cancer from normal peripheral zone and central gland tissue by using dynamic contrast-enhanced MR imaging. Radiology. 2003; 229:248–254. [PubMed: 12944607]
12. Basser PJ, Pierpaoli C. Microstructural and physiological features of tissues elucidated by quantitative-diffusion-tensor MRI. J Magn Reson B. 1996; 111:209–219. [PubMed: 8661285]
13. Song SK, Qu Z, Garabedian EM, Gordon JI, Milbrandt J, Ackerman JJ. Improved magnetic resonance imaging detection of prostate cancer in a transgenic mouse model. Cancer Res. 2002; 62:1555–1558. [PubMed: 11888935]
14. Gibbs P, Tozer DJ, Liney GP, Turnbull LW. Comparison of quantitative T2 mapping and diffusion-weighted imaging in the normal and pathologic prostate. Magn Reson Med. 2001; 46:1054–1058. [PubMed: 11746568]
15. Issa B. In vivo measurement of the apparent diffusion coefficient in normal and malignant prostatic tissues using echo-planar imaging. J Magn Reson Imaging. 2002; 16:196–200. [PubMed: 12203768]
16. Chan I, Wells W III, Mulkern RV, Haker S, Zhang J, Zou KH, Maier SE, Tempany CM. Detection of prostate cancer by integration of line-scan diffusion, T2-mapping and T2-weighted magnetic

resonance imaging; a multichannel statistical classifier. Med Phys. 2003; 30:2390–2398. [PubMed: 14528961]

17. Hosseinzadeh K, Schwarz SD. Endorectal diffusion-weighted imaging in prostate cancer to differentiate malignant and benign peripheral zone tissue. J Magn Reson Imaging. 2004; 20:654. [PubMed: 15390142]
18. Sato C, Naganawa S, Nakamura T, Kumada H, Miura S, Takizawa O, Ishigaki T. Differentiation of noncancerous tissue and cancer lesions by apparent diffusion coefficient values in transition and peripheral zones of the prostate. J Magn Reson Imaging. 2005; 21:258–262. [PubMed: 15723379]
19. Pickles MD, Gibbs P, Sreenivas M, Turnbull LW. Diffusion-weighted imaging of normal and malignant prostate tissue at 3.0T. J Magn Reson Imaging. 2006; 23:130–134. [PubMed: 16374882]
20. Kozlowski P, Chang SD, Jones EC, Berean KW, Chen H, Goldenberg SL. Combined diffusion-weighted and dynamic contrast-enhanced MRI for prostate cancer diagnosis—correlation with biopsy and histopathology. J Magn Reson Imaging. 2006; 24:108–113. [PubMed: 16767709]
21. Gibbs P, Pickles MD, Turnbull LW. Diffusion imaging of the prostate at 3.0 tesla. Invest Radiol. 2006; 41:185–188. [PubMed: 16428991]
22. Griswold MA, Jakob PM, Heidemann RM, Nittka M, Jellus V, Wang J, Kiefer B, Haase A. Generalized autocalibrating partially parallel acquisitions (GRAPPA). Magn Reson Med. 2002; 47:1202–1210. [PubMed: 12111967]
23. Hasan KM, Parker DL, Alexander AL. Comparison of gradient encoding schemes for diffusion-tensor MRI. J Magn Reson Imaging. 2001; 13:769–780. [PubMed: 11329200]
24. Shimony JS, Burton H, Epstein AA, McLaren DG, Sun SW, Snyder AZ. Diffusion tensor imaging reveals white matter reorganization in early blind humans. Cereb Cortex. 2006; 16:1653–1661. [PubMed: 16400157]
25. Stejskal EO, Tanner JE. Spin diffusion measurements: spin echoes in the presence of a time-dependent field gradient. J Chem Phys. 1965; 42:288–292.
26. Humphrey PA, Vollmer RT. Intraglandular tumor extent and prognosis in prostatic carcinoma: application of a grid method to prostatectomy specimens. Hum Pathol. 1990; 21:799–804. [PubMed: 2387573]
27. Xu, J.; Humphrey, PA.; Kibel, AS.; Snyder, AZ.; Narra, VR.; Song, SK. ADC Decrease in histology identified prostate cancer; Proceedings of the 15th Annual Meeting of ISMRM; Berlin, Germany. 2007. p. 3666
28. Budde MD, Kim JH, Liang HF, Schmidt RE, Russell JH, Cross AH, Song SK. Toward accurate diagnosis of white matter pathology using diffusion tensor imaging. Magn Reson Med. 2007; 57:688–695. [PubMed: 17390365]
29. Williams, MC.; Does, MD.; Price, RR. ADC mapping of whole excised human prostate; Proceedings of the 12th Annual Meeting of ISMRM; Kyoto, Japan. 2004. p. 2064
30. Quint LE, Van Erp JS, Bland PH, Del Buono EA, Mandell SH, Grossman HB, Gikas PW. Prostate cancer: correlation of MR images with tissue optical density at pathologic examination. Radiology. 1991; 179:837–842. [PubMed: 2028002]
31. Liney GP, Turnbull LW, Lowry M, Turnbull LS, Knowles AJ, Horsman A. In vivo quantification of citrate concentration and water T2 relaxation time of the pathologic prostate gland using 1H MRS and MRI. Magn Reson Imaging. 1997; 15:1177–1186. [PubMed: 9408138]
32. Chen, AP.; Xu, D.; Henry, R.; Qayyum, A.; Kurhanewicz, J.; Vigneron, DB. Diffusion tensor imaging of the prostate following therapy; Proceedings of the 11th Annual Meeting of ISMRM; Toronto, Ontario, Canada. 2003. p. 579
33. Vigneron, DB.; Xu, D.; Chen, AP.; Swanson, MG.; Kurhanewicz, J. Diffusion tensor imaging of the prostate using single-shot fast spin echo; Proceedings of the 10th Annual Meeting of ISMRM; Honolulu, Hawaii, USA. 2002. p. 457
34. Sinha S, Sinha U. In vivo diffusion tensor imaging of the human prostate. Magn Reson Med. 2004; 52:530–537. [PubMed: 15334571]
35. Reinsberg, SA.; Brewster, JM.; Payne, GS.; Leach, MO.; deSouza, NM. Anisotropic diffusion in prostate cancer: fact or artefact?; Proceedings of the 13th Annual Meeting of ISMRM; Miami Beach, Florida, USA. 2005. p. 269

36. Haker, SJ.; Szot Barnes, A.; Maier, SE.; Tempany, CM.; Mulkern, RV. Diffusion tensor imaging for prostate cancer detection: preliminary results from a biopsy-based assessment; Proceedings of the 13th Annual Meeting of ISMRM; Miami Beach, Florida, USA. 2005. p. 2126

37. Roebuck, JR.; Haker, SJ.; Tempany, CM.; Rybicki, FJ.; Maier, SE.; Mulkern, RV. Diffusion tensor imaging of the prostate: low anisotropies in central gland and peripheral zone in men with adenocarcinoma; Proceedings of the 14th Annual Meeting of ISMRM; Seattle, Washington, USA. 2006. p. 3338

38. Meyer CR, Moffat BA, Kuszpit KK, Bland PL, McKeever PE, Johnson TD, Chenevert TL, Rehemtulla A, Ross BD. A methodology for registration of a histological slide and in vivo MRI volume based on optimizing mutual information. Mol Imaging. 2006; 5:16–23. [PubMed: 16779966]

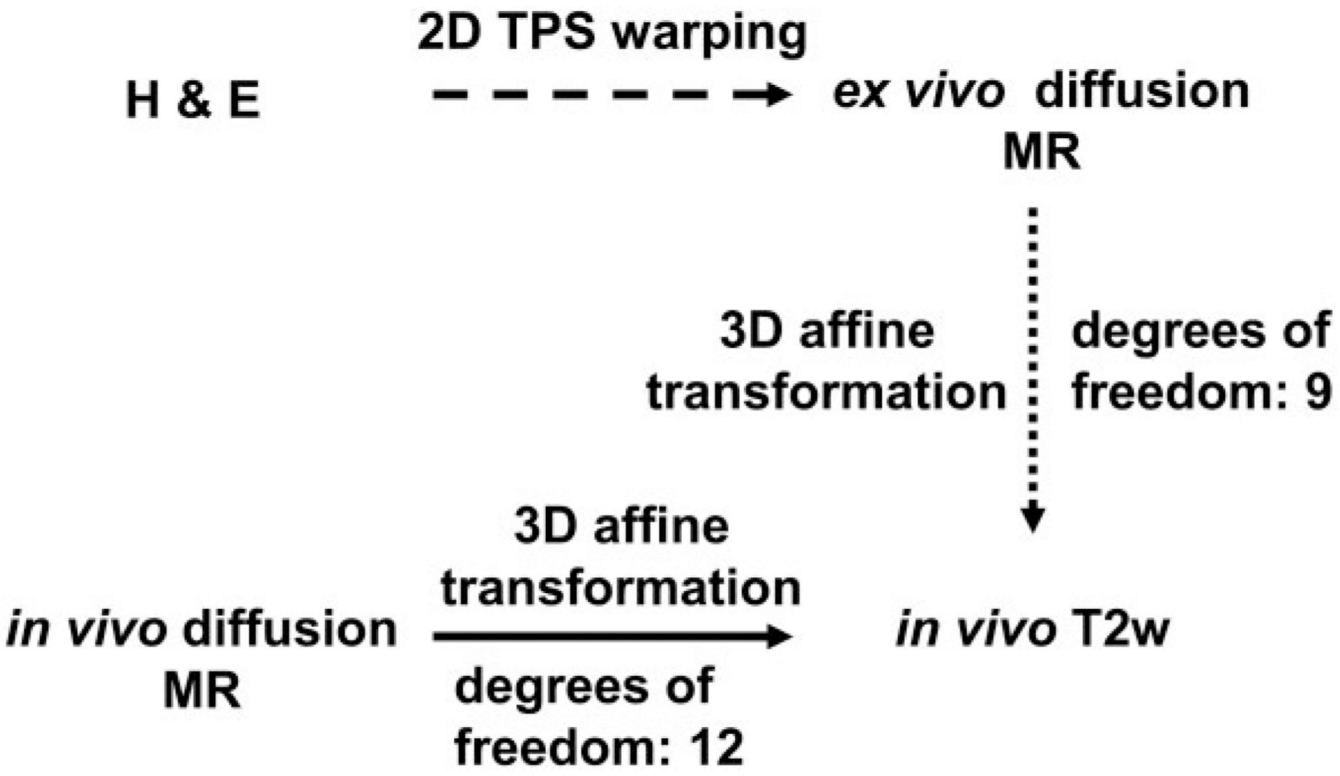

FIG. 1.
Overview of histology and MR coregistration scheme. The dashed line represents the semiautomatic thin plate spline (TPS) warping procedure using manually placed control points. The dotted line represents the manual image registration procedure to transform ex vivo coordinates into in vivo T2w coordinates. The solid line represents the unsupervised in vivo image coregistration procedure.

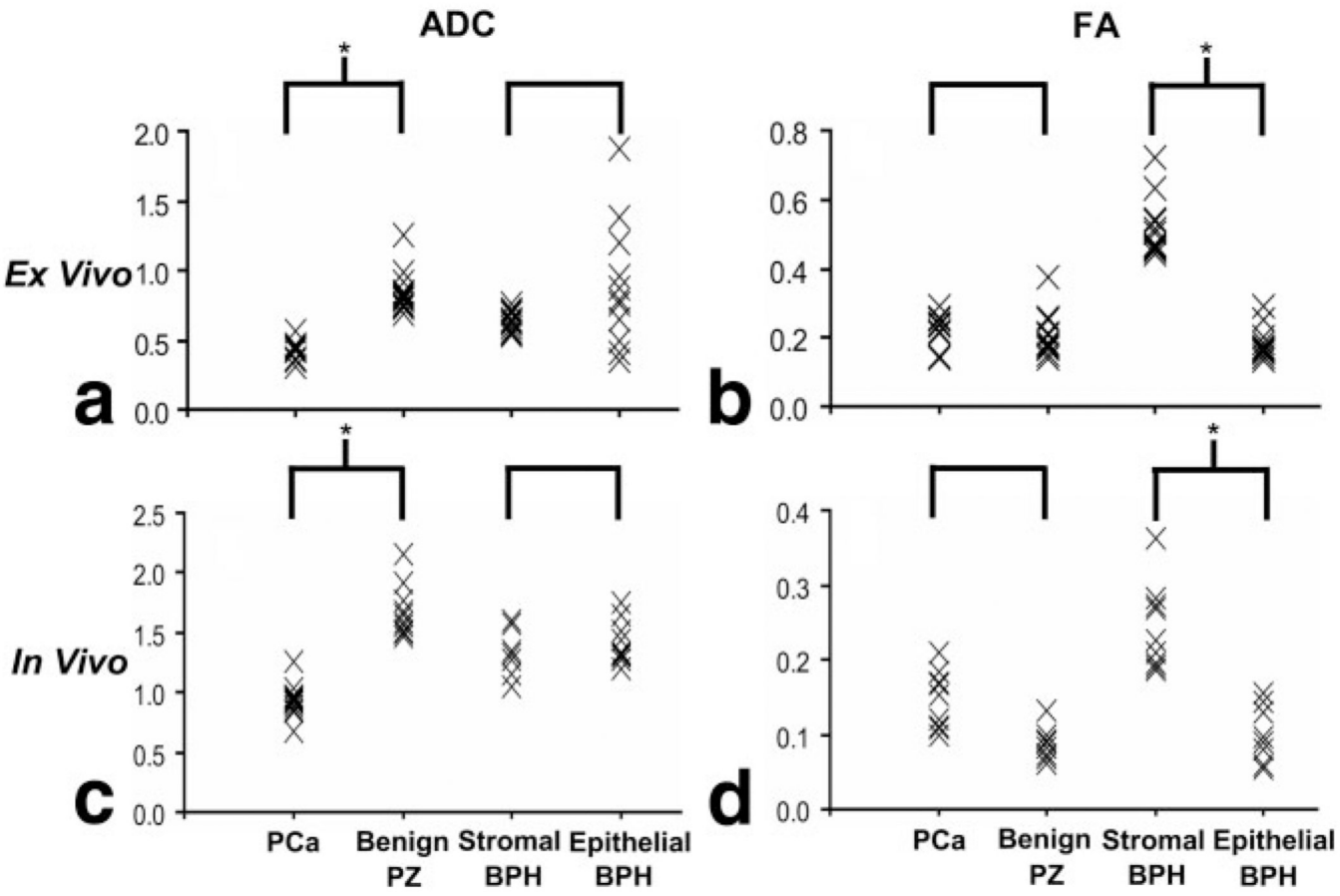

FIG. 2.

a–d: Ex vivo (a,b) and in vivo (c,d) ADC (μm^2/ms; a,c) and FA (unitless; b,d) values for each tissue type: (from left to right in each panel) PCa, benign PZ, stromal BPH, and epithelial BPH. *indicates significant differences ($P < 0.01$).

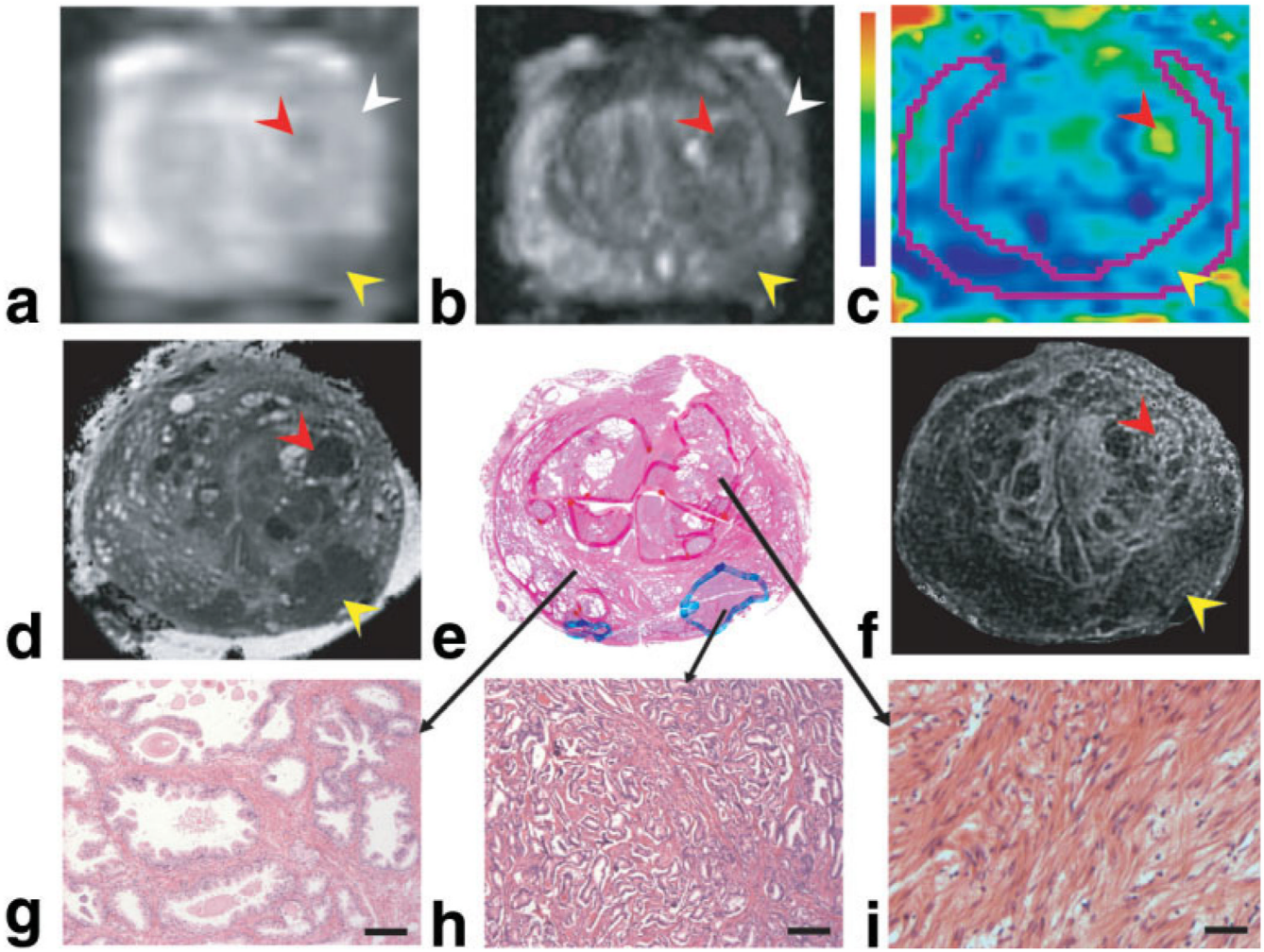

FIG. 3.

Coregistered images illustrate the tissue microstructure underpinning the MR diffusion characteristics: **a:** in vivo ADC (0 –2.0 μm^2/ms); **b:** in vivo T2w; **c:** in vivo color coded FA (0–0.33); **d:** ex vivo ADC (0 –2.0 μm^2/ms); **e:** H&E slide; **f:** ex vivo FA (0–0.79). The cancerous and BPH regions in the H&E slide were marked in blue and red, respectively, by a urologic pathologist. Yellow and red arrows indicate regions of PCa and stromal BPH, respectively, as diagnosed by histology. The white arrow in b indicates a T2 hypointense region that could be mistakenly identified as PCa without the additional coregistered diffusion data. The peripheral zone region was delineated in b and mapped onto c in magenta. **g–i:** High resolution H&E examinations (×10 magnification; scale bar = 100 μm) reveal the microstructures of different types of tissues in (g) benign peripheral zone, (h) PCa, and (i) stromal BPH.

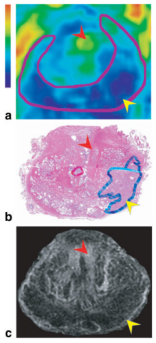

FIG. 4.

One representative case illustrates the lack of diffusion anisotropy differential between benign and cancerous tissue in the peripheral zone. The cancerous and BPH regions in the H&E slides were marked in blue and red, respectively, by a urologic pathologist. Red and yellow arrows indicate regions of fibromuscular hyperplasia (including periurethral muscles merging with anterior stroma) and carcinoma tissues, respectively, as identified by histology. **a:** In vivo FA map (0–0.33). **b:** H&E slide. **c:** Ex vivo FA map (0–0.79). The magenta line in b delineates the peripheral zone as in Figure 2.

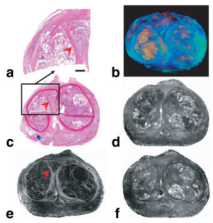

FIG. 5.

One representative case illustrates diffusion anisotropy in a prostate of predominantly epithelial BPH. The cancerous and BPH regions in the H&E slides were marked in blue and red, respectively, by a urologic pathologist. Note that the small cancer was not detected by MR. The region of BPH was largely composed of epithelial nodules with variable size and compactness. Red arrows indicate regions of bundled fibromuscular tissues, respectively, as identified by histology. In panel b, the green (high FA value) regions in the peripheral zone is the result of high FA in the prostate capsule, which in some areas of this case merges with the fibrous tissues surrounding the large BPH nodules. **a:** Magnified right anterior quadrant of the H&E slide (scale bar = 3 mm); **b:** Volume rendered ex vivo DTI image (image scale detailed in the text); **c:** H&E slide; **d:** ex vivo ADC map (0–0.79); **e:** ex vivo FA map (0–2.0 $\mu m^2/ms$); **f:** ex vivo T2w image.

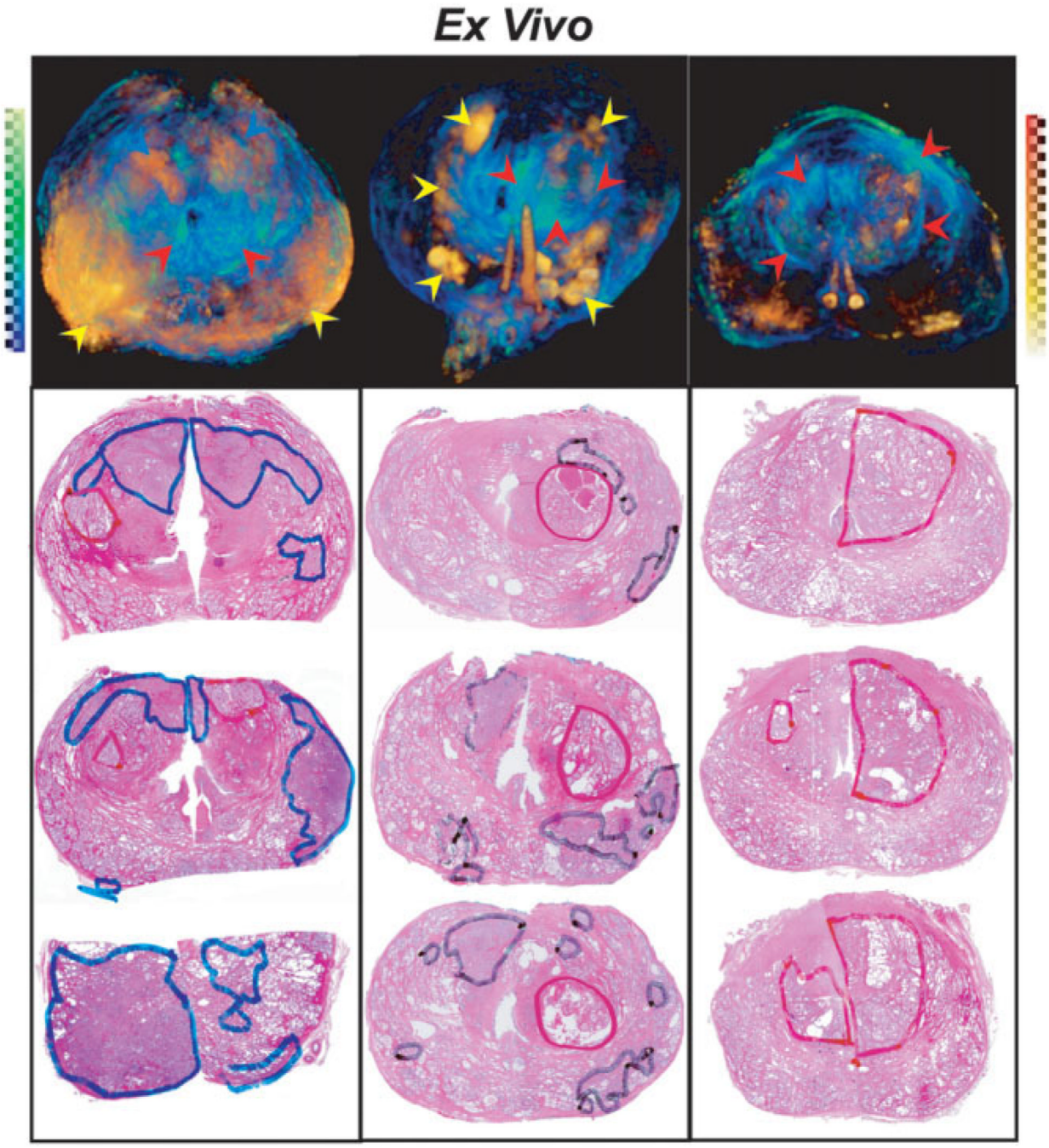

FIG. 6.

Ex vivo diffusion tensor images were coregistered with step-sectioned histology slides from three representative specimens (each column) with different tumor sizes. PCa identified on the volume rendered DTI (projected view) closely correlated with those seen in histology. The histologically defined PCa extents and stages (from left to right in each panel) are 40% T3b, 16% T2c, and 4% T2c. The cancerous and BPH regions in the H&E slides were marked in blue/black and red, respectively, by a urologic pathologist. In the MR images, the ADC (0–0.50 μm^2/ms), and FA (0.39 –1.0) values were imported into the yellow–orange and green–blue channels, respectively. Bright yellow–orange regions in the MR images were identified as carcinoma determined by ADC threshold (ex vivo PCa mean ADC + SD).

Red and yellow arrows indicate regions of fibromuscular and carcinoma tissues, respectively, as identified by both the histology and the coregistered diffusion contrast in the MR images. Pairs of ejaculatory ducts with high ADC value (color scale irrelevant) were segmented from the ADC map separately. Regions of low ADC values at the edge of the prostate specimen in the rightmost case were artifacts caused by air bubbles attached to the prostate capsule.

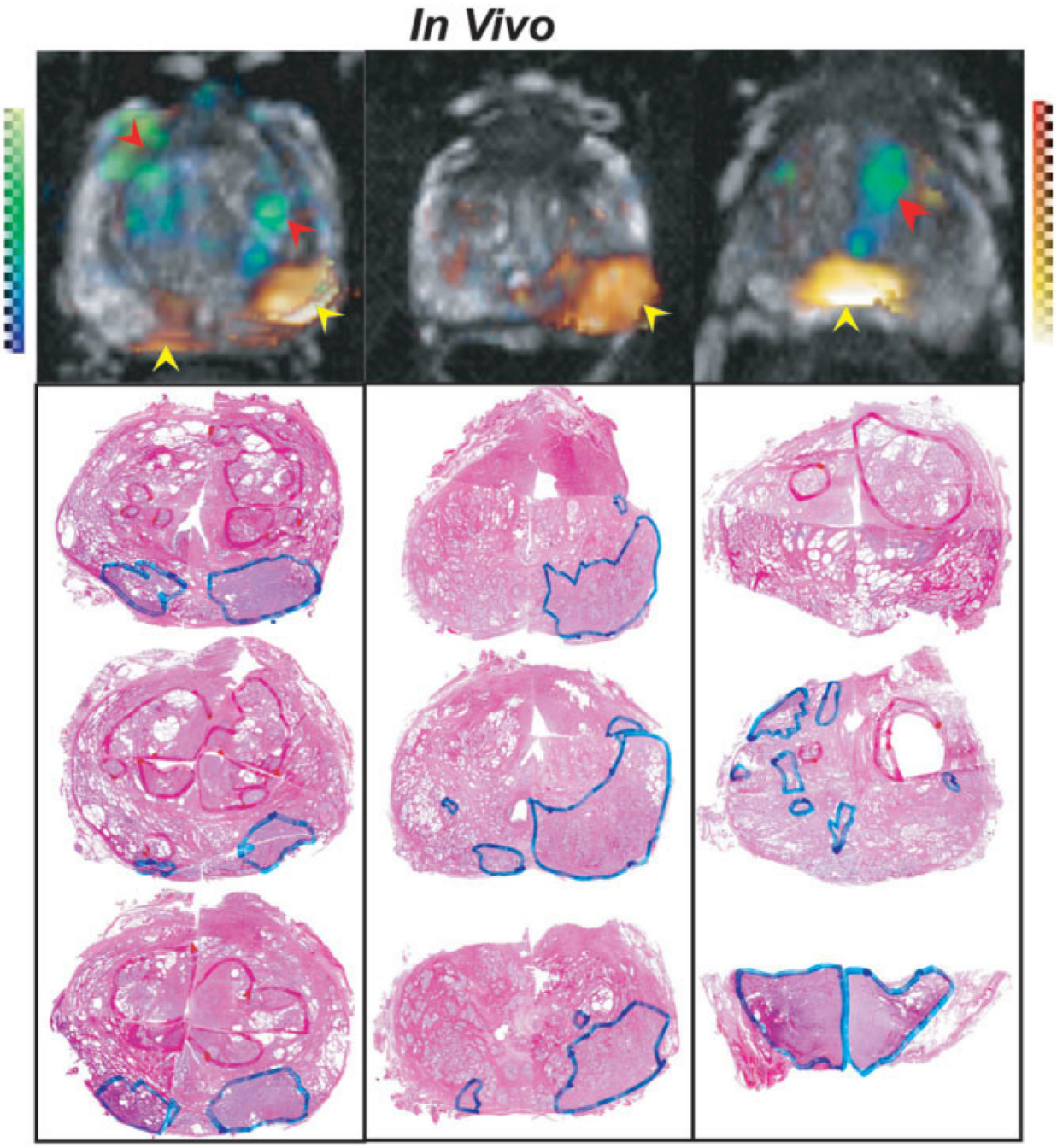

FIG. 7.

In vivo diffusion tensor images were coregistered with step-sectioned histology slides from three representative specimens (each column) with different tumor sizes. PCa identified on the volume rendered DTI (projected view with a representative T2w image as background), closely correlated with those seen in histology. The histologically defined PCa extents and stages (from left to right in each panel) are 15% T3a, 40% T3a, and 20% T3a. The cancerous and BPH regions in the H&E slides were marked in blue and red, respectively, by a urologic pathologist. In the MR images, the ADC (0–1.15 $\mu m^2/ms$), and FA (0–0.41) values were imported into the yellow–orange and green–blue channels, respectively. Bright yellow–orange regions in the MR images were identified as carcinoma determined by ADC

threshold (in vivo PCa mean ADC + SD). Red and yellow arrows indicate regions of fibromuscular and carcinoma tissues, respectively, as identified by both the histology and the coregistered diffusion contrast in the MR images.

Table 1

Tissue Type Classification Combining DTI and T2w Contrasts*

		ADC	FA	T2w
PZ	PCa	hypo	iso	hypo
	Benign	-	-	-
CG	PCa	hypo	iso	hypo
	Stromal BPH	hypo	hyper	hypo
	Epithelial BPH	hetero	iso	hetero
	Benign	-	-	-

* Benign tissues (−) in PZ and CG, respectively, were used as benchmarks for MR contrasts. MR image contrasts were listed as hypo(intense), iso(intense), hyper(intense), or hetero(geneous).